Nano Research
2020, 13(12): 3299–3309
ISSN 1998-0124 CN 11-5974/O4
https://doi.org/10.1007/s12274-020-3006-3

Research Article

Nickel foam supported Cr-doped $NiCo_2O_4$/FeOOH nanoneedle arrays as a high-performance bifunctional electrocatalyst for overall water splitting

Tengyi Liu and Peng Diao (✉)

Key Laboratory of Aerospace Materials and Performance (Ministry of Education), School of Materials Science and Engineering, Beihang University, Beijing 100191, China

Received: 17 May 2020 / **Revised:** 17 July 2020 / **Accepted:** 23 July 2020

ABSTRACT

Efficient and robust noble-metal-free bifunctional electrocatalysts for overall water splitting (OWS) is of great importance to realize the large-scale hydrogen production. Herein, we report the growth of undoped and Cr-doped $NiCo_2O_4$ (Cr-$NiCo_2O_4$) nanoneedles (NNs) on nickel foam (NF) as bifunctional electrocatalysts for both hydrogen evolution reaction (HER) and oxygen evolution reaction (OER). We demonstrate that Cr-doping significantly improves activity for HER and OER by increasing the conductivity of NNs and allowing more active sites on NNs electrochemically accessible. When amorphous FeOOH is electrodeposited on the surface of Cr-$NiCo_2O_4$ NNs, the resulting FeOOH/Cr-$NiCo_2O_4$/NF exhibits itself as an excellent bifunctional catalyst for OWS. In the two-electrode cell where FeOOH/Cr-$NiCo_2O_4$/NF is used both as cathode and anode for OWS, a cell voltage of only 1.65 V is required to achieve an electrolysis current density of 100 mA·cm^{-2}. In addition, the catalyst shows a very high stability for OWS, the two-electrode cell can operate at a consist current density of 20 mA·cm^{-2} for 10 h OWS with the cell voltage being stable at ca. 1.60 V. These results demonstrate that FeOOH/Cr-$NiCo_2O_4$/NF possesses an OWS performance superior to most of transition-metal based bifunctional electrocatalysts working in alkaline medium. The excellent bifunctional activity and stability of FeOOH/Cr-$NiCo_2O_4$/NF are attributed to the following reasons: (i) The NN structure provides a large specific surface area; (ii) the high conductivity of Cr-$NiCo_2O_4$ enables more active centers on the far-end part of NNs to be electrochemically reached; (iii) the deposition of FeOOH supplies additional active sites for OWS.

KEYWORDS

Cr-doped nickel cobaltite, bifunctional electrocatalyst, iron oxyhydroxide, hydrogen evolution reaction, oxygen evolution reaction, overall water splitting

1 Introduction

The increase of both energy consumptions and global environmental issues is stimulating scientists to search for a clean, eco-friendly and renewable energy resource to replace fossil fuels [1–3]. Hydrogen (H_2) has been frequently advocated as a promising energy carrier for its high energy density and zero environmental impact upon combustion [4, 5]. Water electrolysis, which consists of two half reactions: the hydrogen evolution reaction (HER) and the oxygen evolution reaction (OER) [5–7], is widely recognized as an ideal and sustainable way to produce H_2, especially if the electricity can be converted from renewable energy sources such as solar, wind and wave energies [4, 5, 8, 9]. Both HER and OER are uphill reactions [10, 11], and efficient catalysts are necessary to decrease the energy barriers and improve the overall water splitting (OWS) efficiency [11, 12]. At present, noble metal-based catalysts, such as Pt for HER [5, 6], and IrO_2 and RuO_2 for OER [13], are recognized as the state-of-the-art catalysts for electrocatalytic water splitting, because they can deliver high current densities at low overpotentials. Unfortunately, the high cost and intense scarcity of the noble metals have tremendously limited their large-scale industrial applications [5, 6, 12]. In the past decades, tremendous efforts have been devoted to develop the earth-abundant catalysts, including transition metals (TMs) oxides [14–21], chalcogenides [22–26], nitrides [27], phosphides [28], and carbides [6] for HER or OER. Considering the overall efficiency and the cost of electrolysis system, OWS in alkaline medium is more promising than in acidic medium, and the catalysts for both HER and OER in the same electrolyte are preferred for practical applications [7, 10, 29]. Thus, it is crucial to develop low-cost and highly efficient earth-abundant bifunctional electrocatalysts for OWS in alkaline media [9, 10].

Recently, double TM-based oxides, such as $NiFeO_x$ [30–33], $NiCoO_x$ [34, 35], $FeCoO_x$ [36, 37], have been explored extensively as efficient catalysts for HER or OER in alkaline media. Few of them, however, exhibit high activities toward both HER and OER in the same electrolyte environment. As an exception, $NiCo_2O_4$ attracted great attention as a promising catalyst not only because of its bifunctional activity for OWS but also because of its low cost as well as ease preparation [34, 35, 38]. $NiCo_2O_4$-based materials could be fabricated into various nanostructures with high specific surface area, such as $NiCo_2O_4$ nanoneedles (NNs) [39], nanoflakes [34] and nanosheets [38].

Address correspondence to pdiao@buaa.edu.cn

Among them, $NiCo_2O_4$ NNs possessed an extremely high aspect ratios, which can provide more active surface sites per mass unit for electrochemical reactions. However, the low conductivity of $NiCo_2O_4$ NNs seriously hampers their applicability in the electrocatalytic OWS [39–42], because large amounts of active sites are not electrically connected to the supporting electrode due to the high aspect ratio of NNs. Therefore, it is highly desirable to develop a facile method to improve the conductivity of $NiCo_2O_4$ NNs.

Generally, there are two main strategies to improve the conductivity of catalysts: (1) enhancing the intrinsic conductivity in catalysts by inducing dopants into the crystal lattice [7, 17, 43], and (2) employing a well-conductive support that possesses a high specific surface area [10, 44, 45], such as nickel foam (NF) [40] and carbon black [46]. To design a highly active electrocatalyst, it is of great importance to take into account both strategies mentioned above. Recently, Bo et al. [47] fabricated Cr doped Ni-Fe layered double hydroxides (Cr-Ni-Fe LDHs) via a facile co-deposition method. Compared to Ni-Fe LDHs, the obtained Cr-Ni-Fe LDHs catalyst exhibited an enhanced activity toward OER in alkaline solution. More notably, Gong [48] and his co-workers reported Cr-Ni oxides composite that showed a better HER performance than pure Ni oxides in alkaline solution. As reported, Cr^{3+} cations have special electronic configurations ($t_3^{2g}e_0^g$), which is favorable to facilitate electron capture and charge transfer [49, 50]. As a result, the doping of Cr^{3+} cations into Ni or Co oxides will increase their conductivity [49–51]. Hence, it can be reasonably speculated that incorporation of Cr^{3+} into $NiCo_2O_4$ will increase its conductivity, and then activate more active sites on its surface by electrically connecting them to the supporting electrode. In addition, if Cr-doping increases the conductivity of $NiCo_2O_4$ NNs, the activity for OWS can be further improved by modifying the surface of Cr-doped $NiCo_2O_4$ (Cr-$NiCo_2O_4$) NNs with highly active HER and OER cocatalysts.

In this work, we first prepared Cr-doped $NiCo_2O_4$ NNs on NF (Cr-$NiCo_2O_4$/NF) via a facile hydrothermal route followed by annealing. Compared to pristine $NiCo_2O_4$/NF, the Cr-$NiCo_2O_4$/NF electrode exhibits much higher electrocatalytic activity toward HER and OER in alkaline solutions. We demonstrate that the Cr-doping greatly improves the conductivity of nanoneedles, and enables more non-connected active sites on the surface of NNs to be electrochemically accessible. We modified the surface of NNs with iron oxy-hydroxide (FeOOH) and the obtained FeOOH/Cr-$NiCo_2O_4$/NF catalyst exhibits bifunctional activities not only much higher than $NiCo_2O_4$/NF and Cr-$NiCo_2O_4$/NF, but also superior to most of transition-metal based bifunctional electrocatalysts working in alkaline media.

2 Experimental section

2.1 Synthesis of the electrocatalysts

$NiCo_2O_4$ nanoneedles grown on nickel foam ($NiCo_2O_4$/NF): The $NiCo_2O_4$/NF sample was fabricated via a two-step process that was similar to the methods reported in Ref. [52]. NFs (1.5 mm thickness) were first cut into rectangular pieces (5 cm × 2 cm), and then ultrasonicated in 1.37 M HCl for 5 min. After rinsed successively with water (twice), acetone, ethanol, and water (twice), the cleaned NFs were dried in a vacuum oven at 65 °C. The Ni-Co precursor solution was prepared by dissolving 435 mg (1.5 mmol) $Ni(NO_3)_2{\cdot}6H_2O$, 873 mg (3.0 mmol) $Co(NO_3)_3{\cdot}6H_2O$, and 721 mg (12.0 mmol) urea in ultra-pure water (40 mL) under ultrasonication for 10 min. Then, a piece of fresh NF was put into a Teflon-lined stainless-steel autoclave (45 mL) that was filled with 40 mL Ni-Co precursor solution. The autoclave was maintained at 180 °C for 3 h, and then cooled down to room temperature. The sample was rinsed with ethanol and ultra-pure water for several times, and then dried in a vacuum oven at 60 °C for 10 h. Finally, the obtained sample was annealed at 350 °C for 20 min.

Cr-$NiCo_2O_4$/NF: The Cr-$NiCo_2O_4$/NF sample was fabricated via a facile hydrothermal route that is similar to the one used to prepare $NiCo_2O_4$/NF. The only difference was that the hydrothermal precursor solution contained Cr^{3+}. In detail, the hydrothermal precursor solution was prepared by dissolving 435 mg (1.5 mmol) $Ni(NO_3)_2{\cdot}6H_2O$, 815 mg (2.8 mmol) $Co(NO_3)_3{\cdot}6H_2O$, 57 mg (0.2 mmol) $Cr(NO_3)_3{\cdot}6H_2O$, and 721 mg (12.0 mmol) urea in ultra-pure water (40 mL) under ultrasonication for 10 min. Then, a piece of cleaned NF was put into a Teflon-lined stainless-steel autoclave (45 ml) that was filled with 40 mL precursor solution. The autoclave was maintained at 180 °C for 3 h, and then cooled down to room temperature. The sample was rinsed with ethanol and ultra-pure water for several times, and then dried in a vacuum oven at 60 °C for 10 h. Finally, the obtained sample was annealed at 350 °C for 20 min.

FeOOH/Cr-$NiCo_2O_4$/NF: The FeOOH layer was electrodeposited on Cr-$NiCo_2O_4$/NF NNs in 0.1 M $FeCl_2$ solution in 0.1 M $FeCl_2$ solution at 0.3 V vs. SCE for 5 min. The sample was rinsed with ultra-pure water for several times, and then dried in a vacuum oven at 60 °C for 10 h.

Pt/C/NF electrode: The Pt/C powder (2.0 mg, 20 wt.% Pt) was dispersed in the mixed solution of ethanol (1 mL) and Nafion (80 μL) and then ultrasonicated for 15 min to obtain a catalyst ink with a concentration of 2.0 $mg{\cdot}mL^{-1}$. A total amount of 1.0 mg catalyst was loaded onto the surface of NF and the resulting 20 wt.% Pt/C/NF catalyst was dried at room temperature.

$NiCr_2O_4$ grown on nickel foam ($NiCr_2O_4$/NF): The $NiCr_2O_4$/NF sample was fabricated via a facile hydrothermal route followed by annealing. The hydrothermal precursor solution was prepared by dissolving 435 mg (1.5 mmol) $Ni(NO_3)_2{\cdot}6H_2O$, 852 mg (3.0 mmol) $Cr(NO_3)_3{\cdot}6H_2O$, and 721 mg (12.0 mmol) urea in ultra-pure water (40 mL) under ultrasonication for 10 min. Then, a piece of cleaned NF was put into a Teflon-lined stainless-steel autoclave (45 mL) that was filled with 40 mL precursor solution. The autoclave was maintained at 180 °C for 3 h, and then cooled down to room temperature. The sample was rinsed with ethanol and ultra-pure water for several times, and then dried in a vacuum oven at 60 °C for 10 h. Finally, the obtained sample was annealed at 350 °C for 20 min.

The mass of NF and catalyst/NF was measured on a Mettler Toledo XS205DU microbalance with 0.01 mg sensitivity. The loading of catalyst ($mg{\cdot}cm^{-2}$) on NF, which was defined as the mass of grown catalyst ($NiCo_2O_4$ NNs, Cr-$NiCo_2O_4$ NNs, FeOOH/Cr-$NiCo_2O_4$hybrid) per geometric square centimeter, was calculated from the mass change before and after hydrothermal synthesis. The loadings of $NiCo_2O_4$ NNs, Cr-$NiCo_2O_4$ NNs, FeOOH/Cr-$NiCo_2O_4$ hybrid on NF were ~ 1.0 $mg{\cdot}cm^{-2}$.

2.2 Characterizations

The morphologies of the as-prepared catalysts were characterized by using field emission scanning electron microscopy (FESEM, Hitachi S-4800, Japan) operated at an accelerating voltage of 10 kV. X-ray diffraction (XRD) spectra were collected on a Bruker D8 Advance X-ray diffractometer with filtered Cu Kα radiation. X-ray photoelectron spectroscopic (XPS) measurements were carried out on a PHI Quanter a SXM scanning X-ray microprobe (ULVAC-PHI, Japan) at a base pressure of < 10^{-9} Torr. All XPS spectra were obtained with a monochromatic Mg Kα source (1,253.6 eV) and a concentric hemispherical analyzer with a passing energy of 20 eV. Transmission electron microscopy

(TEM) and high-resolution TEM (HRTEM) measurements were performed on a field emission JEM-2100F microscope (JEOL Ltd. Japan) with an accelerating voltage of 200 kV. For TEM characterization, the samples of $NiCo_2O_4$ NNs, Cr-$NiCo_2O_4$ NNs, and FeOOH/Cr-$NiCo_2O_4$ hybrid were scratched off from their corresponding electrodes and dispersed in ethanol under ultrasonication. The resulting suspensions were drop-cast onto copper grid supported carbon film respectively for TEM characterizations. The conductivities of $NiCo_2O_4$ and Cr-$NiCo_2O_4$ powders were measured by using a four-point probe device (Shanghai Qianfeng Co., SQ120/2).

2.3 Electrochemical HER and OER measurements in three-electrode cell

Electrochemical HER and OER measurements were carried out in a typical three-electrode cell connecting with a CHI660A workstation (Shanghai CH Instruments Co. China) at room temperature. The as-prepared FeOOH/Cr-$NiCo_2O_4$/NF, Cr-$NiCo_2O_4$/ NF and $NiCo_2O_4$/NF electrodes were used as working electrodes after cut into a nominal size of 1.0 cm × 1.0 cm with an electrical contact tail that was sealed with paraffin. Electrochemical impedance spectroscopic (EIS) measurements were performed in 1.0 M KOH at overpotential of 0.24 and 0.28 V for HER and OER, respectively, in the frequency range of 10^5 to 10^{-2} Hz with a potential amplitude of 5 mV. While for the measurements of H_2 and O_2 evolution on FeOOH/Cr-$NiCo_2O_4$/NF at constant current, the electrode was cut into a rectangle of 1.0 cm × 0.5 cm. Pt wire and saturated calomel electrode (SCE) were used as the counter and reference electrodes, respectively. Linear sweep voltammetry (LSV) curves were tested in 1.0 M KOH (pH = 14) aqueous solutions with 95% *iR*-compensation at scan rate of 5 $mV \cdot s^{-1}$. Unless noted otherwise, all potentials reported in this work were calibrated with respect to the reversible hydrogen electrode (RHE), and the basic equation was as following

$$E\,(\text{V vs. RHE}) = E\,(\text{V vs. SCE}) + 0.241 + 0.0591\text{pH}$$

2.4 Electrochemical OWS measurements in two-electrode cell

Electrochemical OWS measurements were carried out in a two-electrode cell connecting with a CHI660A workstation (Shanghai CH Instruments Co. China) at room temperature. The as-prepared FeOOH/Cr-$NiCo_2O_4$/NF electrodes (1.0 cm × 1.0 cm) were used as both cathode and anode. One FeOOH/Cr-$NiCo_2O_4$/NF electrode was connected with CHI660A workstation as working electrode, and the other was connected as counter and reference electrode. OWS measurements were carried out in 1.0 M KOH (pH = 14) aqueous solutions.

2.5 Hydrogen and oxygen evolution measurements

The amount of H_2 produced on the FeOOH/$NiCo_2O_4$/NF electrode at a constant current density of −20 $mA \cdot cm^{-2}$ in 1.0 M KOH was measured by using gas chromatography (GC, Tianmei company, GC7890II) with high purity N_2 (containing 2% CH_4) as carrier gas. The FeOOH/$NiCo_2O_4$/NF electrode had a geometric area of of 1.0 cm × 0.5 cm. The electrolysis measurements were carried out in a special three-compartment electrochemical cell.

The three compartments were connected at the bottom and the compartment for the working electrode had an air-inlet tube reaching to the bottom and a top opening that could be sealed from air with a rubber stopper. Before measurements, the electrolyte was bobbled with N_2 for 30 min to remove dissolved oxygen in solution and air in the compartments. The gas sample was taken from the working electrode chamber with a gas tight syringe through the sealed rubber cap at electrolysis time of 5, 10, 15, 20, 25, and 30 min. The evolution of H_2 was calculated out by integrating the peak area in GC spectra. The relationship between the peak area of H_2 in GC spectra and the actual H_2 amount was firstly calibrated using Pt electrode. The theoretically expected evolution of H_2 at constant *j* of −20 $mA \cdot cm^{-2}$ was calculated according to Faraday's law, and the Faradic efficiency for HER at working electrode was estimated by comparing the measured and calculated values.

The amount of O_2 produced on the FeOOH/$NiCo_2O_4$/NF electrode at a constant current density of 20 $mA \cdot cm^{-2}$ in 1.0 M KOH was measured by using O_2 fluorescence detector (Ocean Optics, R-sensor) in the working electrode compartment. Before measurements, the working electrode compartment was purged with N_2 for 30 min. During the oxygen evolution at a constant *j* of 20 $mA \cdot cm^{-2}$ for 30 min, the amount of O_2 on the FeOOH/$NiCo_2O_4$/NF was directly measured by the O_2 sensor. The theoretically expected evolution of O_2 at constant *j* of 20 $mA \cdot cm^{-2}$ was calculated according to Faraday's law, and the Faradic efficiency for OER at working electrode was estimated by comparing the measured and calculated values.

3 Results and discussion

3.1 Morphology and structure of the FeOOH/Cr-$NiCo_2O_4$/NF catalyst

Scheme 1 shows the schematic diagram of the preparation of the FeOOH/Cr-$NiCo_2O_4$/NF electrode. Briefly, Cr-$NiCo_2O_4$ NNs were directly synthesized on commercial NF via a hydrothermal process followed by annealing treatment. Then, amorphous FeOOH layer was electrodeposited onto the surface of as-prepared Cr-$NiCo_2O_4$/NF to obtain the FeOOH/Cr-$NiCo_2O_4$/NF hybrid. For comparison, undoped $NiCo_2O_4$/NF was also prepared via the same method but without adding Cr source in hydrothermal precursor solution. XRD spectra (Fig. 1(a)) confirm the crystal phase of three examined catalysts is cubic spinel $NiCo_2O_4$ (PDF#20-781). Compared to pristine $NiCo_2O_4$, Cr-doped sample shows an obvious negative shift in the peak position of (311) and (440), while the peaks corresponding to metallic Ni (NF) exhibit no shift. According to the Bragg equation [53], these peak-shifts toward lower diffraction angle

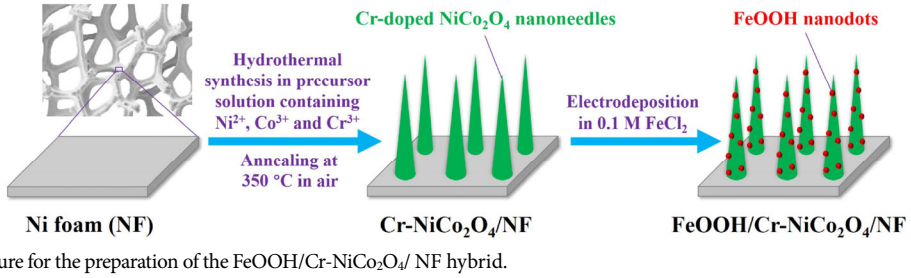

Scheme 1 The procedure for the preparation of the FeOOH/Cr-$NiCo_2O_4$/ NF hybrid.

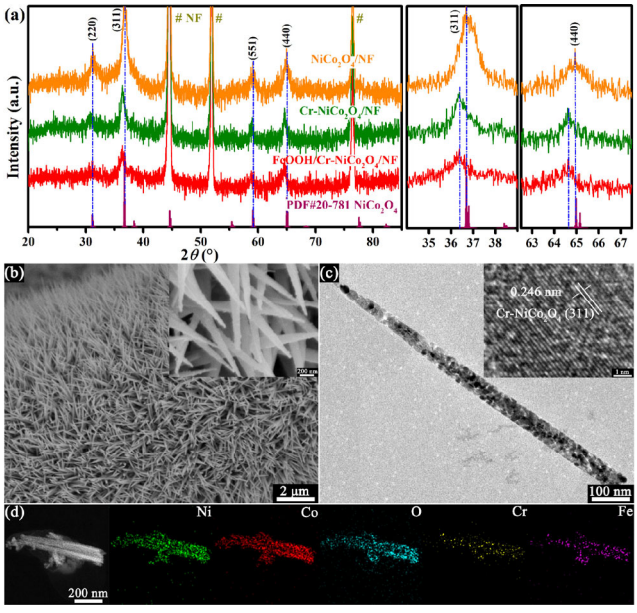

Figure 1 (a) XRD patterns of $NiCo_2O_4$/NF, Cr-$NiCo_2O_4$/NF, and FeOOH/Cr-$NiCo_2O_4$/NF. (b) Typical SEM images of FeOOH/Cr-$NiCo_2O_4$. Inset: local magnification. (c) Typical TEM image of a single FeOOH/Cr-$NiCo_2O_4$ nanoneedle. Inset: HRTEM image. (d) Elemental mapping images of FeOOH/Cr-$NiCo_2O_4$ NN.

imply that the lattice spacing of $NiCo_2O_4$ is increased after Cr-doping. As is well known, the atomic radius of Cr is larger than those of Ni and Co [50, 51], and Cr^{3+} has a larger ionic radius (0.62 Å) than Co^{3+} (0.52 Å). Therefore, the doping of Cr into $NiCo_2O_4$ catalyst will lead to detectable structural distortion and enlarge the lattice spacing. XPS survey spectra (Fig. S1 in the Electronic Supplementary Material (ESM)) also confirm the existence of Cr element in doped samples. Figure S2 in the ESM presents the typical SEM images of $NiCo_2O_4$ and Cr-$NiCo_2O_4$ grown on NF. We can clearly see that both $NiCo_2O_4$ and Cr-$NiCo_2O_4$ are composed of NNs standing vertically to the substrate, in good agreement with previous studies [34]. This result indicates that Cr-doping did not influence the needle-like morphology of $NiCo_2O_4$. To study their crystal structure, the $NiCo_2O_4$ and Cr-$NiCo_2O_4$ NNs were scratched off from NF and characterized by HRTEM (Fig. S3 in the ESM). HRTEM images show that the lattice spacing of (311) planes in Cr-$NiCo_2O_4$ is 0.246 nm, which is slightly larger than that (0.245 nm) of undoped $NiCo_2O_4$, agreeing well the XRD result that Cr-doping induced an expanded crystal lattice.

FeOOH, as an efficient OER catalyst [36], was electrodeposited onto the surface of Cr-$NiCo_2O_4$ NNs to prepare the FeOOH/Cr-$NiCo_2O_4$/NF hybrid. The XPS survey spectrum (Fig. S1(c) in the ESM) confirms the appearance of Fe on the resulting hybrid, indicating the successful deposition of FeOOH on Cr-$NiCo_2O_4$/NF. Figure 1(a) presents the XRD spectrum of FeOOH/Cr-$NiCo_2O_4$/NF, which displays the same diffraction pattern as that of Cr-$NiCo_2O_4$/NF and no diffraction features of FeOOH are identified. This observation indicates that the electrodeposited FeOOH has an amorphous nature, which is well consistent with the previous reports [35, 54]. Figure 1(b) shows the typical SEM images of FeOOH/Cr-$NiCo_2O_4$/NF, from which it is clearly seen that the NNs grew uniformly on the whole substrate with high density, implying that the electrodeposition of FeOOH has little effect the needle-like morphology of Cr-$NiCo_2O_4$. The high-magnification SEM image (inset of Fig. 1(b)) shows that the hybrid NNs are coated by numerous nanodots as compared to Cr-$NiCo_2O_4$ NNs, which provides direct evidence for the existence of FeOOH on the surface of Cr-$NiCo_2O_4$. Typical TEM image of a single FeOOH/Cr-$NiCo_2O_4$ NN (Fig. 1(c)) reveals that the NNs are not composed of a single crystal but composed of small connected domains. This phenomenon was also observed on the undoped and Cr-doped $NiCo_2O_4$ NNs (see Figs. S3(a) and S3(c) in the ESM). The HRTEM image (inset of Fig. 1(c)) shows that these domains are single crystalline grains with a lattice spacing of 0.246 nm, in good agreement with that of (311) planes of cubic spinel Cr-$NiCo_2O_4$. FeOOH nanodots were hardly identified in TEM images because of their amorphous nature. To confirm the presence of FeOOH nanodots, energy-dispersive X-ray spectroscopy (EDX) elemental mapping was carried out on FeOOH/Cr-$NiCo_2O_4$ NNs, and the results are shown in Fig. 1(d). We can clearly see that the hybrid contains the elements of Ni, Co, O, Cr and Fe, which is well consistent with the XPS results. Figure 1(d) also demonstrates the uniform spatial distribution of each element on FeOOH/Cr-$NiCo_2O_4$ NNs. Meanwhile, the EDX spectrum (Fig. S4 in the ESM) provides the precise atomic ratios of the component elements in FeOOH/Cr-$NiCo_2O_4$ NNs. The atomic ratio of Ni, Co and O elements is 1:2:4, which is in good agreement with the chemical formula of $NiCo_2O_4$, and their total atomic ratios are much larger than that of Cr and Fe elements. This observation is due to the fact that $NiCo_2O_4$ was employed as the base material, and the amounts of Cr and Fe introduced into $NiCo_2O_4$ were much smaller as compared to the base material.

3.2 Electrocatalytic activity of the FeOOH/Cr-$NiCo_2O_4$/NF catalyst toward HER

The electrocatalytic activity of all catalysts for HER was examined using LSV in 1.0 M KOH solution. Figure 2(a) shows the current density (j) vs. potential (V) curves of $NiCo_2O_4$/NF, Cr-$NiCo_2O_4$/NF, and FeOOH/Cr-$NiCo_2O_4$/NF. $NiCo_2O_4$/NF shows a low activity for HER due to its poor conductivity, which hinders the active sites located on upper ends of NNs to be well connected to the conductive NF substrate. As mentioned before, Cr^{3+} cations were doped into the crystal structure of $NiCo_2O_4$/NF to improve its conductivity and then to enhance the activity. As expected, Cr-doped $NiCo_2O_4$/NF exhibits much higher activity for HER than undoped $NiCo_2O_4$/NF. For example, $NiCo_2O_4$/NF has a current density of ca. -18 mA·cm^{-2} at -0.227 V, whereas after Cr doping, the resulting Cr-$NiCo_2O_4$/NF exhibits a current density of -100 mA·cm^{-2} at the same potential, which is over 5 times higher than that on $NiCo_2O_4$/NF. This observation suggests that Cr doping can greatly improve the activity of $NiCo_2O_4$ NNs toward HER.

In addition, we also examined the electrocatalytic activity of Cr-$NiCo_2O_4$ NNs catalysts with different Cr-doping amount (see Fig. S5 in the ESM). The activity for HER first increased and then decreased with the increase of Cr amounts from 0 to 0.4 mmol in hydrothermal precursor solution, and reached the highest value at the Cr amount of 0.2 mmol. This phenomenon is due to the fact that the activity depends on the number of accessible surface active sites, which is dominated by the following two factors: (1) high electrochemical surface area, and (2) excellent conductivity. The moderate Cr-doping amount in Cr-$NiCo_2O_4$ NNs will not only improve the conductivity but also retain the needle-like morphology. Whereas, the excessive dopant amount of Cr in Cr-$NiCo_2O_4$ will destroy the needle-like morphology (see Fig. S6 in the ESM), leading to a decline in activity for electrocatalytic water splitting. Thus, in this work, the precursor solution containing 0.2 mmol Cr^{3+} was used to prepare the Cr-$NiCo_2O_4$/NF catalysts.

As we aimed at developing bifunctional catalyst, FeOOH, a good electrocatalyst for OER [36], was electrodeposited on the

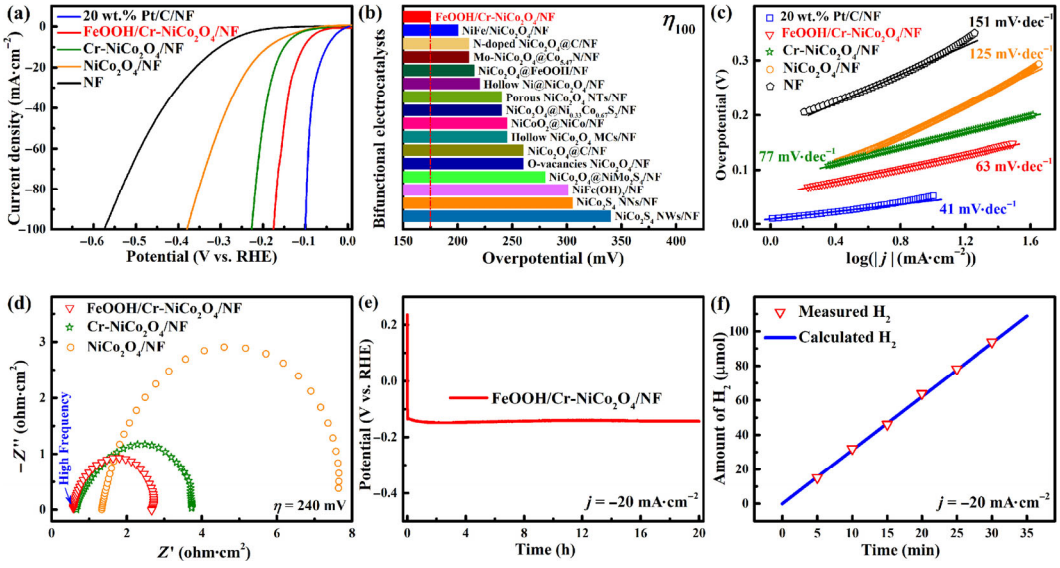

Figure 2 Electrocatalytic performance of $NiCo_2O_4$/NF, Cr-$NiCo_2O_4$/NF, and FeOOH/Cr-$NiCo_2O_4$/NF for HER in 1.0 M KOH. (a) LSV curves obtained at a potential sweep rate of 5 mV·s^{-1}. (b) Comparison of the overpotentials obtained on our and reported bifunctional electrocatalysts to deliver a current density of 100 mA·cm^{-2} for HER. (c) Tafel plots. (d) EIS spectra obtained at the overpotential of 240 mV in 1.0 M KOH in the frequency range from 10^5 to 10^{-2} Hz with a potential amplitude of 5 mV. (e) Potential–time curve obtained on FeOOH/Cr-$NiCo_2O_4$/NF at a constant current density of −20 mA·cm^{-2}. (f) Comparison of the calculated (blue solid line) and the measured (red open triangles) amount of H_2 on the FeOOH/Cr-$NiCo_2O_4$/NF electrode with a geometric size of 1.0 cm × 0.5 cm.

surface of Cr-$NiCo_2O_4$ to improve the OER performance. However, to our surprise, the obtained FeOOH/Cr-$NiCo_2O_4$/NF hybrid exhibited an unexpectedly improved activity for HER, as shown in Fig. 2(a). The onset potential of FeOOH/Cr-$NiCo_2O_4$/NF is significantly positive-shifted as compared to those of $NiCo_2O_4$/NF and Cr-$NiCo_2O_4$/NF, indicating that FeOOH/Cr-$NiCo_2O_4$/NF has the highest activity for HER among all examined catalysts. Usually, the overpotentials (η) at absolute current density ($|j|$) of 10, 20, 50, and 100 mA·cm^{-2} (denoted as η_{10}, η_{20}, η_{50}, η_{100}, respectively) are employed to quantitatively assess the activity of catalysts for HER or OER. As listed in Table S1 in the ESM, the values of η_{10}, η_{20}, η_{50} and η_{100} obtained on FeOOH/Cr-$NiCo_2O_4$/NF are 104, 124, 151 and 175 mV, respectively, which are much smaller than the corresponding ones obtained on $NiCo_2O_4$/NF and Cr-$NiCo_2O_4$/NF. For comparison, Table S1 in the ESM also lists the values of η_{10}, η_{20}, η_{50} and η_{100} reported in literature on other NF supported bifunctional catalysts [40, 52, 55–69]. To make the comparison more intuitive, we plotted η_{100} of our hybrid and other typical electrocatalysts in Fig. 2(b). By contrast, FeOOH/Cr-$NiCo_2O_4$/NF exhibits the lowest η_{100} of 175 mV to obtain a j value of 100 mA·cm^{-2}, providing strong evidence that our hybrid is one of the most active bifunctional catalysts for HER [40, 52, 55–69].

Tafel plots were presented to study the kinetics of electrocatalytic HER on our FeOOH/Cr-$NiCo_2O_4$/NF catalyst. Figure 2(c) shows the linear regions of Tafel plots obtained on all examined catalysts, from which the Tafel slopes of NF, $NiCo_2O_4$/NF, Cr-$NiCo_2O_4$/NF, FeOOH/Cr-$NiCo_2O_4$/NF and 20% Pt/C/NF catalysts are 151, 125, 77, 63 and 41 mV·dec^{-1}, respectively. As is well-known, a smaller Tafel slope means a faster increasing rate of current density with the increase of overpotential [5]. The Tafel slope of Cr-$NiCo_2O_4$/NF (77 mV·dec^{-1}) is nearly one-half of that of $NiCo_2O_4$/NF (125 mV·dec^{-1}), indicating that Cr-doping greatly improved the conductivity of $NiCo_2O_4$ and then led to a higher activity toward HER. Moreover, compared to Cr-$NiCo_2O_4$/NF, FeOOH/Cr-$NiCo_2O_4$/NF possesses an even smaller Tafel slope of 63 mV·dec^{-1}, suggesting that modifying Cr-$NiCo_2O_4$ with FeOOH can further enhance the HER performance. Notably, the Tafel slope of 63 mV·dec^{-1} reveals that HER proceeded via a Volmer-Heyrovsky mechanism on our FeOOH/Cr-$NiCo_2O_4$/NF catalyst.

EIS measurements were performed to investigate the Faradic charge transfer resistance of HER ($R_{ct\text{-}HER}$) and the ohmic resistance (R_{ohm}) of the electrode/solution system. Figure 2(d) displays the Nyquist plots of the $NiCo_2O_4$/NF, Cr-$NiCo_2O_4$/NF, and FeOOH/Cr-$NiCo_2O_4$/NF electrodes at overpotential of 240 mV. All three electrodes show semicircles in the Nyquist plots, indicating that Faradic charge transfer process is the rate-determining step in HER. As is well known, the intercept of the semicircle with the real axis (Z') in the high frequency region reflects R_{ohm} that involves the solution resistance (R_s) in series with the electrode resistance (R_e, resistance of electron flow from the conducting NF substrate to active sites on catalyst), and therefore R_{ohm} equals to the sum of R_s and R_e ($R_{ohm} = R_s + R_e$). As shown in Fig. 2(d), the Cr-doped samples (Cr-$NiCo_2O_4$/NF and FeOOH/Cr-$NiCo_2O_4$/NF) have the same R_{ohm} value of 0.63 ohm·cm^{-2}, which is only one-half of the value obtained on the undoped sample ($NiCo_2O_4$/NF). Because R_s kept unchanged during EIS measurements, the smaller R_{ohm} value of Cr-doped samples provides a direct experimental evidence that Cr-doping greatly decreased R_e by improving the conductivity of Cr-doped catalysts. In addition, the diameter of the semicircle in Figure 2(d) reflects the charge transfer resistance (here, $R_{ct\text{-}HER}$), and the smaller the diameter, the faster the charge transfer reaction. The Cr-$NiCo_2O_4$/NF catalyst exhibits a much smaller value of $R_{ct\text{-}HER}$ (2.97 ohm·cm^2,) than that (6.36 ohm·cm^2,) of the undoped $NiCo_2O_4$/NF, indicating that the activity for HER was greatly improved by Cr-doping. We believe that the improved activity of Cr-$NiCo_2O_4$/NF comes from the Cr-doping induced enhancement of conductivity, which enables more active sites located on far end of NNs to be electrically connected to the conducting NF substrate. It should be pointed out, as shown in Fig. 2(d), modifying Cr-$NiCo_2O_4$/NF with FeOOH can further reduce $R_{ct\text{-}HER}$ to 2.18 ohm·cm^2. This observation suggests that the deposited FeOOH nanodots on Cr-$NiCo_2O_4$/NF also offers reaction centers for HER, resulting in a faster charge transfer reaction. Taken together, these results provide strong support that FeOOH/Cr-$NiCo_2O_4$/NF electrode displays an excellent activity toward HER.

Long-term stability is an extremely important criterion for HER catalysts. To evaluate the long-term stability of our FeOOH/Cr-$NiCo_2O_4$/NF electrode, chronopotentiometric measurements were conducted in 1.0 M KOH at a current density of −20 mA·cm^{-2} for 20 h, and the corresponding potential–time curve is shown in Fig. 2(e). It is well-known that, while the electrocatalytic activity of a cathode decays during galvanostatic reduction, the potential will increase with reaction time. From Fig. 2(e), we can clearly see that the applied potential was stabilized at ca. −0.13 V vs. RHE. Moreover, after the long-term water electrolysis, we observed that there was no catalyst peeling off from the electrode in the solution. In addition, continuous cyclic voltammetric (CV) measurements and large constant current (−100 mA·cm^{-2}) measurements were carried out to further examine the stability of the hybrid catalyst for HER, and the results are shown in Figs. S7(a) and S7(b) in the ESM. We can clearly see that the LSV curves of the hybrid catalyst before and after 1,000 cycles of continuous CV sweeps coincide well with each other, demonstrating high durability of the catalyst for HER. Moreover, the potential remained stable at ca. −0.18 V vs. RHE during the large constant current (−100 mA·cm^{-2}) measurements. These results provide solid evidence that our FeOOH/Cr-$NiCo_2O_4$/NF electrode has an excellent stability for long-term HER.

The Faradic efficiency for H_2 evolution is another important parameter to evaluate the electrocatalytic activity of an electrode toward HER. We measured the amount of H_2 produced at a constant j of −20 mA·cm^{-2} in a sealed electrochemical cell by using gas chromatography (see Experimental section for more details). The theoretically expected amount of H_2 at constant j of −20 mA·cm^{-2} can also be calculated according to Faraday's law, and the result is shown in Fig. 2(f). The good coincidence of calculated and measured evolution of H_2 indicates that almost all current was used to generate H_2, and the Faradic efficiency for HER on FeOOH/Cr-$NiCo_2O_4$/NF electrode is nearly 100%.

3.3 Electrocatalytic activity of the FeOOH/Cr-$NiCo_2O_4$/NF catalyst toward OER

We also investigated the electrocatalytic activity of the FeOOH/Cr-$NiCo_2O_4$/NF catalyst toward OER. Figure 3(a) compares the LSV curves of FeOOH/Cr-$NiCo_2O_4$/NF with those of $NiCo_2O_4$/NF and Cr-$NiCo_2O_4$/NF. The undoped $NiCo_2O_4$/NF shows an OER onset potential of about 1.53 V vs. RHE, while the Cr-doped sample (Cr-$NiCo_2O_4$/NF) shows a much smaller one (1.47 V vs. RHE), indicating that Cr-doping of $NiCo_2O_4$/NF can also greatly improve the activity toward OER. Notably, decorating Cr-$NiCo_2O_4$/NF with FeOOH can further reduce the OER onset potential to 1.44 V vs. RHE. This is not surprising considering that FeOOH is an efficient OER catalyst [36]. As shown clearly in Fig. 3(a), the three catalysts exhibited activity for OER in the order FeOOH/Cr-$NiCo_2O_4$/NF > Cr-$NiCo_2O_4$/NF > $NiCo_2O_4$/NF, which is the same as the activity order for HER. To quantitatively evaluate the activity, the OER overpotentials (η_{10}, η_{20}, η_{50} and η_{100}) obtained on the above examined catalysts are listed in Table S2 in the ESM, and the corresponding values reported on other bifunctional catalysts in literature are also presented for comparison [40, 52, 55–69]. As listed in Table S2 in the ESM, FeOOH/Cr-$NiCo_2O_4$/NF exhibits the η_{10}, η_{20}, η_{50} and η_{100} values of 217, 235, 254 and 268 mV to deliver current densities of 10, 20, 50 and 100 mA·cm^{-2}. For an intuitive comparison, the value of η_{100} on different bifunctional catalysts was presented in the histogram shown in Fig. 3(b). By contrast, the values of η_{100} and other overpotentials (η_{10}, η_{20} and η_{50}) are the smallest among the corresponding values shown in Fig. 3(b) or listed in Table S2 in the ESM [40, 52, 55–69], indicating that our FeOOH/Cr-$NiCo_2O_4$/NF is superior to other bifunctional catalysts reported previously in literature.

Figure 3(c) shows the Tafel plots of blank NF, $NiCo_2O_4$/NF, Cr-$NiCo_2O_4$/NF, and FeOOH/Cr-$NiCo_2O_4$/NF, from which the Tafel slopes of the corresponding catalysts are obtained to be 105, 62, 42, and 31 mV·dec^{-1}, respectively. Among the above three catalysts, FeOOH/Cr-$NiCo_2O_4$/NF exhibits the smallest Tafel slope of 31 mV·dec^{-1}, and this value is also the smallest among those reported on other bifunctional catalysts listed in Table S2 in the ESM. We believe the high activity of FeOOH/Cr-$NiCo_2O_4$/NF for OER is mainly due to the fact that the deposition of FeOOH induced more active sites on the surface of Cr-$NiCo_2O_4$/NF. We also notice that the Tafel slope of Cr-$NiCo_2O_4$/NF (42 mV·dec^{-1}) is much smaller than that of $NiCo_2O_4$/NF (62 mV·dec^{-1}), suggesting that Cr-doping also contributes to the improvement of OER activity (Fig. 3(c)).

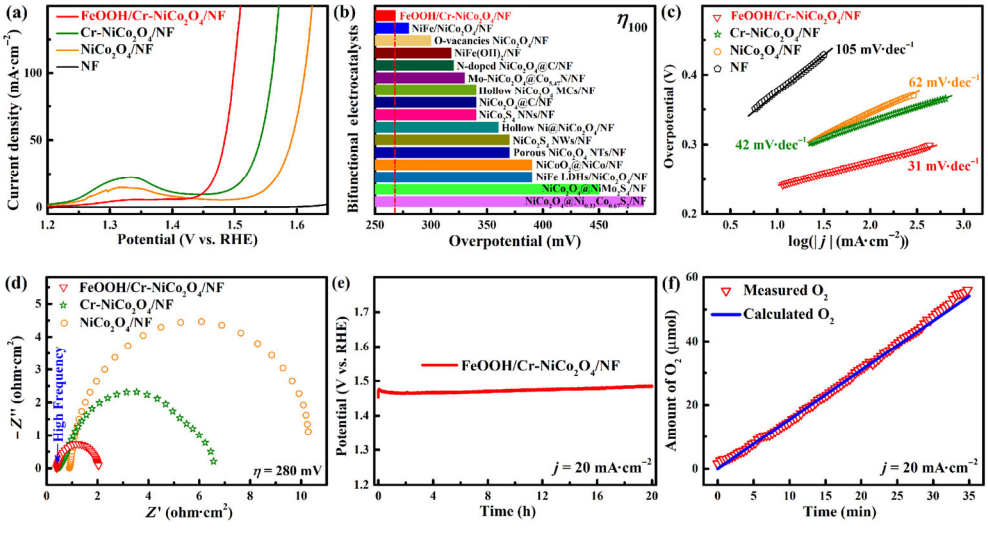

Figure 3 Electrocatalytic performance of $NiCo_2O_4$/NF, Cr-$NiCo_2O_4$/NF, and FeOOH/Cr-$NiCo_2O_4$/NF for OER in 1.0 M KOH. (a) LSV curves obtained at a potential sweep rate of 5 mV·s^{-1}. (b) Comparison of the overpotentials obtained on our and reported bifunctional electrocatalysts to deliver a current density of 100 mA·cm^{-2} for OER. (c) Tafel plots. (d) EIS spectra obtained at the overpotential of 280 mV in 1.0 M KOH in the frequency range from 10^5 to 10^{-2} Hz with a potential amplitude of 5 mV. (e) Potential–time curve obtained on FeOOH/Cr-$NiCo_2O_4$/NF at a constant current density of 20 mA·cm^{-2}. (f) Comparison of the calculated (blue solid line) and the measured (red open triangles) amount of O_2 on the FeOOH/Cr-$NiCo_2O_4$/NF electrode with a geometric size of 1.0 cm × 0.5 cm.

We believe that the reason why Cr-doping increases the OER activity of the doped samples is the same as that it increases the HER activity. In other words, Cr-doping boosts both HER and OER activity via increasing the conductivity of $NiCo_2O_4$, resulting in more active sites being electrically connected to NF substrate.

EIS measurements were carried out to provide evidence that the conductivity of $NiCo_2O_4$/NF was improved via Cr-doping. Figure 3(d) shows the EIS plots of three $NiCo_2O_4$-based electrodes at an anodic η of 280 mV (1.51 V vs. RHE). It can be clearly seen that the Cr-doped samples (both Cr-$NiCo_2O_4$/NF and FeOOH/Cr-$NiCo_2O_4$/NF) possess the same R_{ohm} value that is only one-half of the value of pure $NiCo_2O_4$/NF. This result reveals that Cr-doping greatly decreases the inter-domain resistance of the Cr-doped catalysts by increasing their conductivity. Meanwhile, the Faradic charge transfer resistances of OER ($R_{ct\text{-}OER}$) on $NiCo_2O_4$/NF, Cr-$NiCo_2O_4$/NF and FeOOH/ Cr-$NiCo_2O_4$/NF were obtained from the diameter of corresponding semicircles, which are 9.65, 6.17 and 2.12 ohm·cm^{-2}, respectively, suggesting that their activity toward OER increases in the order $NiCo_2O_4$/NF < Cr-$NiCo_2O_4$/NF < FeOOH/Cr-$NiCo_2O_4$/NF. On the basis of the above results, we can safely conclude that the FeOOH/Cr-$NiCo_2O_4$/NF catalyst displayed an excellent activity toward OER due to following two reasons: (1) Cr-doping and (2) FeOOH modification. The former improved the conductivity of Cr-$NiCo_2O_4$ and then activated more active sites by electrically-connecting them to the conducting NF substrate, while the latter introduced large amounts of highly active FeOOH nanodots on the surface of Cr-$NiCo_2O_4$/NF.

We also evaluate the long-term stability of our FeOOH/Cr-$NiCo_2O_4$/NF catalyst for OER. Figure 3(e) displays the potential–time curve in 1.0 M KOH at a constant current density of 20 mA·cm^{-2} for 20 h. The applied potential was stabilized at ca. 1.47 V vs. RHE during 20 h electrolysis, exhibiting an excellent stability for long-term water oxidation. The coincidence of LSV curves before and after continuous 1,000 cycles of CV measurements and the stable potential during the large constant-current measurements (100 mA·cm^{-2}) further confirm the high-performance stability of the catalyst during water oxidation (shown in Figs. S8(a) and S8(b) in the ESM). Moreover, to estimate the Faradic efficiency, we used an O_2 sensor in the gas-tight electrochemical cell to measure the evolution of oxygen. Figure 3(f) compares the measured and the calculated evolution of O_2 during OER at constant current density of 20 mA·cm^{-2}. The coincidence of the two lines indicates that nearly all currents were used to produce O_2, and the Faradic efficiency is close to 100% for oxygen evolution.

3.4 Overall water splitting performance of FeOOH/Cr-$NiCo_2O_4$/NF in two-electrode cell

All the above results indicate that FeOOH/Cr-$NiCo_2O_4$/NF is a highly efficient and stable electrocatalyst for both HER and OER in alkaline solution. In order to evaluate the bifunctional activity for overall water splitting, we used a double-electrode cell with our FeOOH/Cr-$NiCo_2O_4$/NF electrodes as both the cathode and the anode. For comparison, we also tested the bifunctional performance of the $NiCo_2O_4$/NF and Cr-$NiCo_2O_4$/NF catalysts, and the results are shown in Fig. 4(a). It can be observed that our FeOOH/Cr-$NiCo_2O_4$/NF catalyst exhibits a bifunctional electrocatalytic activity superior to the other two. For example, to deliver a current density of 100 mA·cm^{-2}, $NiCo_2O_4$/NF and Cr-$NiCo_2O_4$/NF required a cell voltage of ~ 2.01 and ~ 1.79 V, respectively, while FeOOH/Cr-$NiCo_2O_4$/NF required only ~ 1.65 V. This value is also the lowest among the cell voltages reported recently on other $NiCo_2O_4$-based bifunctional electrocatalysts (Fig. 4(b)) [40, 52, 55–69]. Table 1 lists the cell voltages needed by our catalysts to supply an OWS current density of 10, 20, 50, and 100 mA·cm^{-2}. For ease comparison, the corresponding values reported in literature on other $NiCo_2O_4$-based bifunctional catalysts are also presented in Table 1. It is clearly seen that, to deliver a high current density (> 50 mA·cm^{-2}) for OWS, our FeOOH/Cr-$NiCo_2O_4$/NF catalyst exhibits the smallest cell voltage among all the listed bifunctional catalysts [40, 52, 55–69].

It should be pointed out herein, that the broad oxidation peaks on the $NiCo_2O_4$/NF and Cr-$NiCo_2O_4$/NF electrodes at potentials before OER in Fig. 3(a) disappear in Fig. 4(a). This observation is a common phenomenon for bifunctional catalysts for OWS. As reported in previous literature, many bifunctional catalysts exhibit obvious oxidation peaks before OER in LSV curves when they were used as working electrodes in a three-electrode cell. However, when these catalysts were employed as both cathode and anode in a two-electrode cell for OWS, their LSV curves for OWS demonstrate no oxidation peak [40, 49, 62, 69]. We believe this observation is due to the difference between the three-electrode and the two-electrode setups. As is well known, for the LSV curves obtained with the standard three-electrode cells, the current density is reported with respect to the reference electrode that has a constant potential. In other works, the abscissa in Fig. 3(a) is the potential difference against RHE. Whereas, in the two-electrode cells, the counter electrode is also employed as the reference electrode, and the potential of which cannot be kept constant due to the passing current. Therefore, the abscissa in Fig. 4(a) is not the potential with respect to a reference electrode, but the total cell voltage between cathode and anode.

Meanwhile, we also tested the long-term stability of FeOOH/Cr-$NiCo_2O_4$/NF in 1.0 M KOH at a constant current density of 20 mA·cm^{-2} for 10 h, and the result is shown in Fig. 4(c). We can clearly see that, during the 10 h constant current electrolysis, the cell voltage was stabilized at ~ 1.60 V, providing a solid evidence that our FeOOH/Cr-$NiCo_2O_4$/NF catalyst possesses

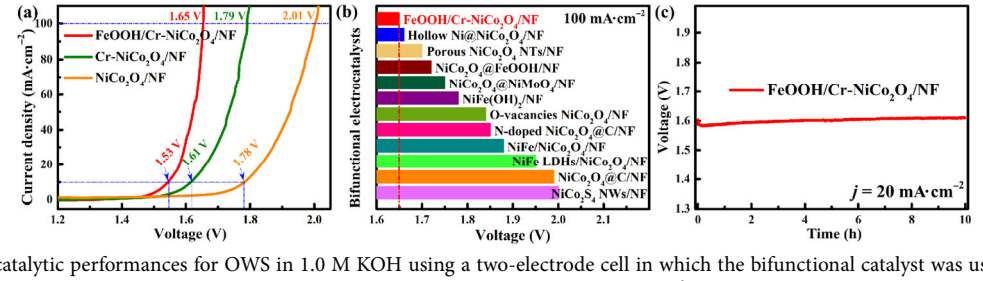

Figure 4 Electrocatalytic performances for OWS in 1.0 M KOH using a two-electrode cell in which the bifunctional catalyst was used as both cathode and anode. (a) LSV curves. (b) Comparison of the cell voltages at a current density of 100 mA·cm^{-2} for OWS. The data of the other catalysts are extracted from the published literature listed in Table 1. (c) Constant current electrolysis at a current density of 20 mA·cm^{-2} using FeOOH/Cr-$NiCo_2O_4$/NF as both cathode and anode.

Table 1 Overall water splitting performance of the two-electrode cell with the $NiCo_2O_4$-based bifunctional electrocatalyst acting as both cathode and anode in 1.0 M KOH[a]

Ref.	Materials	Loading ($mg \cdot cm^{-2}$)	Cell voltage to supply a current density (V)			
			10 ($mA \cdot cm^{-2}$)	20 ($mA \cdot cm^{-2}$)	50 ($mA \cdot cm^{-2}$)	100 ($mA \cdot cm^{-2}$)
TW*	FeOOH/Cr-$NiCo_2O_4$/NF	1.0	1.53	1.57	1.62	1.65
TW	Cr-$NiCo_2O_4$/NF	1.0	1.61	1.66	1.73	1.79
TW	$NiCo_2O_4$/NF	1.0	1.78	1.83	1.91	2.01
[52]	Porous $NiCo_2O_4$ NTs/NF	—	—	1.63	1.66	1.70
[55]	Hollow $NiCo_2O_4$ MCs/NF	1.0	1.65	1.74	—	—
[56]	O-vacancy $NiCo_2O_4$/NF	2.5	1.61	1.69	1.76	1.84
[57]	N-doped $NiCo_2O_4$@C/NF	28.0	1.43	1.52	1.68	1.85
[58]	$NiCo_2O_4$@C/NF	1.0	1.61	1.70	1.85	1.99
[59]	Hollow Ni@$NiCo_2O_4$/NF	—	1.58	1.61	1.64	1.66
[60]	$NiCoO_2$@NiCo/NF	4.0	1.69	1.79	1.91	—
[61]	Mo-$NiCo_2O_4$@$Co_{5.47}N$/NF	1.0	1.56	~ 1.64	~ 1.75	—
[62]	$NiCo_2O_4$&$Ni_{0.33}Co_{0.67}S_2$/NF	0.3	~ 1.71	1.78	—	—
[63]	$NiCo_2O_4$@$NiMoO_4$/NF	—	1.55	1.65	—	—
[64]	$NiCo_2O_4$@$NiMo_2S_4$/NF	2.4	—	—	1.63	1.75
[65]	NiFe LDHs/$NiCo_2O_4$/NF	4.9	1.60	1.67	1.81	1.95
[40]	NiFe/$NiCo_2O_4$/NF	—	1.67	1.71	1.79	1.88
[66]	$NiCo_2O_4$@FeOOH/NF	—	1.52	—	1.63	1.72
[67]	$NiFe(OH)_2$/NF	4.7	1.67	1.69	~ 1.72	~ 1.78
[68]	$NiCo_2S_4$ NNs/NF	0.43	1.68	~ 1.82	—	—
[69]	$NiCo_2S_4$ NWs/NF	—	1.63	~ 1.73	~ 1.91	~ 2.0

[a]TW: this work; NTs: nanotubes; MCs: microcuboids; NWs: nanowires.

an excellent stability for OWS in alkaline solution.

3.5 Origin of the high bifunctional activity of the FeOOH/Cr-$NiCo_2O_4$/NF catalyst

Figure 5(a) displays the high-resolution XPS spectra of $NiCo_2O_4$ NNs, Cr-$NiCo_2O_4$ NNs and FeOOH/Cr-$NiCo_2O_4$ NNs. Deconvolution of the spectra demonstrates that both Co $2p_{3/2}$ and Co $2p_{1/2}$ peaks contain signals from Co^{3+} and Co^{2+}. Pure $NiCo_2O_4$ possesses much larger peak areas of Co^{3+} as compared to that of Co^{2+}, which indicates that Co^{3+} is the dominant state in $NiCo_2O_4$. However, both Cr-doped catalysts (Cr-$NiCo_2O_4$ and FeOOH/Cr-$NiCo_2O_4$) show that the peak-area of Co^{2+} is much larger than that of Co^{3+}. We estimated the atomic percentage of Co^{3+} and Co^{2+} before and after Cr-doping on the basis of peak areas of Co^{3+} and Co^{2+} in Fig. 5(a). The undoped $NiCo_2O_4$ has a Co^{3+} percentage of 68.5% and a Co^{2+} percentage of 31.5%. However, the percentages of Co^{3+} in Cr-doped samples are significantly decreased, and the percentages of Co^{2+} are increased to ~ 62.8% for Cr-$NiCo_2O_4$ and ~ 63.1% for FeOOH/Cr-$NiCo_2O_4$. Previous studies reported that the conductivity of Co-based materials is closely related to the ratio of internal Co^{2+}/Co^{3+}, and higher concentration of Co^{2+} results in a better conductivity of catalyst [14, 51, 64, 65]. We believe that this is because Co^{2+} is likely to convert to Co^{3+} while releasing one free electron into the catalyst. Therefore, Co^{2+} in $NiCo_2O_4$ and Cr-$NiCo_2O_4$ acts as electron donor, and a higher concentration of Co^{2+} will inevitably lead to a larger free electron density. Accordingly, these results provide direct evidence that Cr-doping greatly increases the concentrations of Co^{2+} in Cr-$NiCo_2O_4$, and then improves the conductivity by increasing the free electron density.

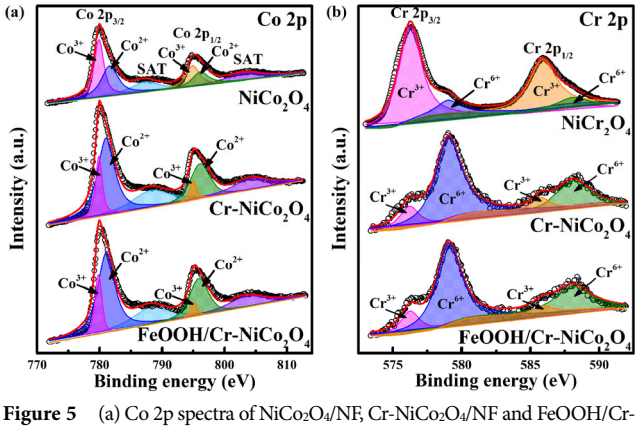

Figure 5 (a) Co 2p spectra of $NiCo_2O_4$/NF, Cr-$NiCo_2O_4$/NF and FeOOH/Cr-$NiCo_2O_4$/NF, (b) Cr 2p spectra of $NiCr_2O_4$/NF, Cr-$NiCo_2O_4$/NF and FeOOH/Cr-$NiCo_2O_4$/NF.

To explore why Cr-doping significantly improves the concentration of Co^{2+} in Cr-$NiCo_2O_4$, we examined the XPS spectra of Cr 2p (Fig. 5(b)). Both Cr-$NiCo_2O_4$ and FeOOH/Cr-$NiCo_2O_4$ exhibit two sets of doublet peaks that correspond to the Cr $2p_{3/2}$ and Cr $2p_{1/2}$ states of Cr^{3+} and Cr^{6+}, respectively. For ease comparison, we also prepared pure $NiCr_2O_4$ and its XPS spectrum is presented in Fig. 5(b). It is clearly seen that pure $NiCr_2O_4$ has a ~ 12.8% atomic percentage of Cr^{6+} in total Cr. In contrast, the Cr-$NiCo_2O_4$ and FeOOH/Cr-$NiCo_2O_4$ have an over 67.0% (~ 67.4% and ~ 67.5%) atomic percentage of Cr^{6+}, respectively. This observation suggests that more Cr atom presented itself as Cr^{6+} in Cr-$NiCo_2O_4$. These results indicate that, as a dopant, Cr mainly exists as Cr^{6+} in Cr-$NiCo_2O_4$ due to following electron transfer reaction: $3Co^{3+} + Cr^{3+} \rightarrow 3Co^{2+} + Cr^{6+}$. Taken together, it can be concluded that the Cr dopants act as electron donors and significantly improve the conductivity of the Cr-doped catalysts by increasing their electron density.

To examine the conductivity of $NiCo_2O_4$ before and after Cr doping, we measured the resistivity of $NiCo_2O_4$ and Cr-$NiCo_2O_4$ by using the four-point probe method (see the ESM for more details). The obtained potentials and calculated resistivity of $NiCo_2O_4$ and Cr-$NiCo_2O_4$ are listed in Table S3 in the ESM.

The resistivity values of $NiCo_2O_4$ and Cr-$NiCo_2O_4$ are 2.01 × 10^{-3} and 9.74 × 10^{-4} ohm·m, which is in good agreement with the results of nickel- and cobalt-based oxides in Refs. [70, 71]. Because conductivity is inversely proportional to resistivity, it is reasonable to conclude that the Cr doping significantly improved the conductivity of Cr-$NiCo_2O_4$.

It is self-evident that, for a high-aspect-ratio NNs array electrode, the specific surface area (A_{SSA}) is not equal to the real electrochemical surface area (A_{ECSA}) especially when the conductivity of NNs is significantly changed. This is because the far-end part of NNs may not well electrically connected to the supporting electrodes. Therefore, to explore the origin of the electrocatalytic activity of our catalysts, it is essential to reveal the relation between A_{SSA} and A_{ECSA}. We measured A_{SSA} of our catalysts by using Brunauer–Emmett–Teller (BET) method, and the results are shown in Fig. S9 in the ESM. The A_{SSA} values of $NiCo_2O_4$/NF and Cr-$NiCo_2O_4$/NF are 923.9 and 938.3 $cm^2 \cdot cm^{-2}$ (note: $cm^2 \cdot cm^{-2}$ refers to the area obtained in one unit geometric area of NF), respectively. $NiCo_2O_4$/NF and Cr-$NiCo_2O_4$/NF had almost the same A_{SSA} value, indicating that Cr-doping has no effect on the morphology of NNs.

However, the A_{ECSA} value of Cr-doped catalyst may be quite different from the undoped one because Cr-doping improves the conductivity of NNs and then leads to the increase of electrochemical surface area on NNs. Accordingly, we measured A_{ECSA} of our catalysts by recording the CV curve at different potential sweep rates (v) in an inert potential window, and the charging current density (j_c) can be obtained from the CV curves (Fig. S10 in the ESM). As $j_c = vC_{dl}$, where C_{dl}, is the double layer capacitance of electrode, and the value of C_{dl} can be obtained from the $j_c \sim v$ plot. Figure 6 displays the $j_c \sim v$ plots of different catalysts and their corresponding linear fittings, from which the C_{dl} values of $NiCo_2O_4$/NF, Cr-$NiCo_2O_4$/NF and FeOOH/Cr-$NiCo_2O_4$/NF are obtained as 10.8, 23.1 and 24.4 $mF \cdot cm^{-2}$, and the corresponding A_{ECSA} values are calculated to be 270, 577.5 and 610 $cm^2 \cdot cm^{-2}$, respectively, on the basis of the following equation: $A_{ECSA} = C_{dl}/C_0$, where C_0 is the specific capacitance of an ideally planar surface electrode whose value is taken as 0.04 $mF \cdot cm^{-2}$ [12, 51]. Due to the poor conductivity of $NiCo_2O_4$ NNs, its A_{ECSA} is only ca. 29.2% of A_{SSA}, implying that a large part of the surface of $NiCo_2O_4$ NNs cannot be electrochemically reached. However, for Cr-$NiCo_2O_4$ NNs, A_{ECSA} is ca. ~ 61.5% of A_{SSA}, which is more than two-fold of the value of $NiCo_2O_4$ NNs. This is because Cr-doping can greatly improve the conductivity of $NiCo_2O_4$ NNs, which allows more surface parts to be electrochemically reached.

Scheme 2 shows the schematic illustrations of the surface active sites at the $NiCo_2O_4$/NF, Cr-$NiCo_2O_4$/NF and FeOOH/Cr-$NiCo_2O_4$/NF electrodes. As for the $NiCo_2O_4$/NF electrode, many surface active sites are not electrically connected to

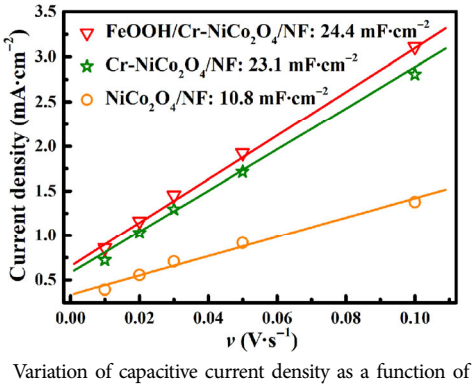

Figure 6 Variation of capacitive current density as a function of potential sweep rate on $NiCo_2O_4$/NF, Cr-$NiCo_2O_4$/NF, and FeOOH/Cr-$NiCo_2O_4$/NF.

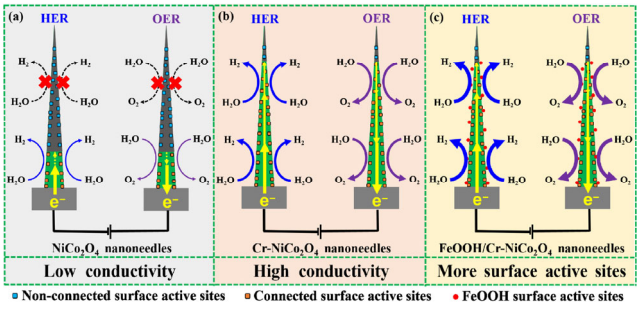

Scheme 2 Schematic illustrations of nanoneedles and active sites on (a) $NiCo_2O_4$/NF, (b) Cr-$NiCo_2O_4$/NF, and (c) FeOOH/Cr-$NiCo_2O_4$/NF.

the conducting NF substrate due to the poor conductivity of $NiCo_2O_4$ NNs (Scheme 2(a)), leading to a low activity for OWS. While for the Cr-$NiCo_2O_4$/NF electrode, the good conductivity allows more surface actives sites be electrochemically accessible (Scheme 2(b)), and as a result, the electrocatalytic activity of Cr-$NiCo_2O_4$/NF is greatly improved. As shown in Scheme 2(c), the electrodeposited FeOOH nanodots provide additional active sites for OER and HER. Therefore, the FeOOH/Cr-$NiCo_2O_4$/NF catalyst exhibits the best performance for OWS in this two-electrode cell. The excellent bifunctional electrocatalytic activity of the FeOOH/Cr-$NiCo_2O_4$/NF electrode is attributed to the following three factors: (i) The densely grown NNs provide a large specific surface area; (ii) the good conductivity of Cr-$NiCo_2O_4$ activates more active sites on the surface of NNs; and (iii) the appearance of FeOOH supplies further reaction centers for OWS.

4 Conclusions

In summary, we have designed and fabricated the NF supported Cr-$NiCo_2O_4$ NNs, which shows enhanced bifunctional electrocatalytic activity for both HER and OER compared to the undoped $NiCo_2O_4$/NF in alkaline solutions. Doping $NiCo_2O_4$ with Cr greatly improves the conductivity of NNs, allowing more non-connected active sites in the far-end of NNs to be electrochemically accessible and then enhancing the activity. Amorphous FeOOH nanodots were electrodeposited onto Cr-$NiCo_2O_4$/NF to further increase the number of active surface sites. The obtained FeOOH/Cr-$NiCo_2O_4$/NF catalyst exhibits higher bifunctional activities compared to $NiCo_2O_4$/NF and Cr-$NiCo_2O_4$/NF. When acting as a cathode for HER, it delivers current densities of −10, −50 and −100 $mA \cdot cm^{-2}$ at overpotentials of only 104, 151 and 175 mV, respectively. While acting as an anode for OER, it requires overpotentials of only 217, 254 and 268 mV to achieve current densities of 10, 50 and 100 $mA \cdot cm^{-2}$, respectively. In a two-electrode cell where FeOOH/Cr-$NiCo_2O_4$/NF is used both as cathode and anode for OWS, cell voltages as low as 1.53 and 1.65 V are needed to achieve current densities of 10 and 100 $mA \cdot cm^{-2}$, respectively. Moreover, long-term constant current measurement shows that FeOOH/Cr-$NiCo_2O_4$/NF possesses an excellent stability for OWS. The high performance for OWS demonstrates that FeOOH/Cr-$NiCo_2O_4$/NF is one of the most efficient bifunctional catalysts working in alkaline medium.

Acknowledgements

We gratefully acknowledge the financial support of this work by the National Natural Science Foundation of China (Nos. 51872015 and 51672017).

Electronic Supplementary Material: Supplementary material (XPS spectra of different electrodes, SEM and TEM images of

different electrodes, EDX data of the hybrid sample, Tables for comparing the performance of $NiCo_2O_4$-based bifunctional catalysts for HER and OER, BET curves of different electrodes, and CV curves on different electrodes at different potential sweep rates) is available in the online version of this article at https://doi.org/10.1007/s12274-020-3006-3.

References

[1] Steinberg, M. Fossil fuel decarbonization technology for mitigating global warming. *Int. J. Hydrogen Energy* **1999**, *24*, 771–777.

[2] Crabtree, G. W.; Dresselhaus, M. S.; Buchanan, M. V. The hydrogen economy. *Phys. Today* **2004**, *57*, 39–44.

[3] Gasteiger, H. A.; Marković, N. M. Just a dream—Or future reality? *Science* **2009**, *324*, 48–49.

[4] Lewis, N. S.; Nocera, D. G. Powering the planet: Chemical challenges in solar energy utilization. *Proc. Natl. Acad. Sci. USA* **2006**, *103*, 15729–15735.

[5] Zou, X. X.; Zhang, Y. Noble metal-free hydrogen evolution catalysts for water splitting. *Chem. Soc. Rev.* **2015**, *44*, 5148–5180.

[6] Chen, W. F.; Muckerman, J. T.; Fujita, E. Recent developments in transition metal carbides and nitrides as hydrogen evolution electrocatalysts. *Chem. Commun.* **2013**, *49*, 8896–8909.

[7] You, B.; Sun, Y. J. Innovative strategies for electrocatalytic water splitting. *Acc. Chem. Res.* **2018**, *51*, 1571–1580.

[8] Walter, M. G.; Warren, E. L.; McKone, J. R.; Boettcher, S. W.; Mi, Q. X.; Santori, E. A.; Lewis, N. S. Solar water splitting cells. *Chem. Rev.* **2010**, *110*, 6446–6473.

[9] Gandía, L. M.; Oroz, R.; Ursúa, A.; Sanchis, P.; Diéguez, P. M. Renewable hydrogen production: Performance of an alkaline water electrolyzer working under emulated wind conditions. *Energy Fuels* **2007**, *21*, 1699–1706.

[10] Yan, Y.; Xia, B. Y.; Zhao, B.; Wang, X. A review on noble-metal-free bifunctional heterogeneous catalysts for overall electrochemical water splitting. *J. Mater. Chem. A* **2016**, *4*, 17587–17603.

[11] Morales-Guio, C. G.; Stern, L. A.; Hu, X. L. Nanostructured hydrotreating catalysts for electrochemical hydrogen evolution. *Chem. Soc. Rev.* **2014**, *43*, 6555–6569.

[12] McCrory, C. C. L.; Jung, S.; Ferrer, I. M.; Chatman, S. M.; Peters, J. C.; Jaramillo, T. F. Benchmarking hydrogen evolving reaction and oxygen evolving reaction electrocatalysts for solar water splitting devices. *J. Am. Chem. Soc.* **2015**, *137*, 4347–4357.

[13] Suen, N. T.; Hung, S. F.; Quan, Q.; Zhang, N.; Xu, Y. J.; Chen, H. M. Electrocatalysis for the oxygen evolution reaction: Recent development and future perspectives. *Chem. Soc. Rev.* **2017**, *46*, 337–365.

[14] Xiao, Z. H.; Wang, Y.; Huang, Y. C.; Wei, Z. X.; Dong, C. L.; Ma, J. M.; Shen, S. H.; Li, Y. F.; Wang, S. Y. Filling the oxygen vacancies in Co_3O_4 with phosphorus: An ultra-efficient electrocatalyst for overall water splitting. *Energy Environ. Sci.* **2017**, *10*, 2563–2569.

[15] Klaus, S.; Cai, Y.; Louie, M. W.; Trotochaud, L.; Bell, A. T. Effects of Fe electrolyte impurities on $Ni(OH)_2$/NiOOH structure and oxygen evolution activity. *J. Phys. Chem. C* **2015**, *119*, 7243–7254.

[16] Gong, M.; Dai, H. J. A mini review of NiFe-based materials as highly active oxygen evolution reaction electrocatalysts. *Nano Res.* **2015**, *8*, 23–39.

[17] Vojvodic, A.; Norskov, J. K.; Abild-Pedersen, F. Electronic structure effects in transition metal surface chemistry. *Top. Catal.* **2014**, *57*, 25–32.

[18] Xu, Y. F.; Gao, M. R.; Zheng, Y. R.; Jiang, J.; Yu, S. H. Nickel/nickel(II) oxide nanoparticles anchored onto cobalt(IV) diselenide nanobelts for the electrochemical production of hydrogen. *Angew. Chem., Int. Ed.* **2013**, *52*, 8546–8550.

[19] Zhang, J.; Dong, C. Q.; Wang, Z. B.; Gao, H.; Niu, J. Z.; Peng, Z. Q.; Zhang, Z. H. A new defect-rich CoGa layered double hydroxide as efficient and stable oxygen evolution electrocatalyst. *Small Methods* **2019**, *3*, 1800286.

[20] Friebel, D.; Louie, M. W.; Bajdich, M.; Sanwald, K. E.; Cai, Y.; Wise, A. M.; Cheng, M. J.; Sokaras, D.; Weng, T. C.; Alonso-Mori, R. et al. Identification of highly active Fe sites in (Ni,Fe)OOH for electrocatalytic water splitting. *J. Am. Chem. Soc.* **2015**, *137*, 1305−1313.

[21] Zhang, J.; Bai, Y. W.; Zhang, C.; Gao, H.; Niu, J. Z.; Shi, Y. J.; Zhang, Y.; Song, M. J.; Zhang, Z. H. Hybrid $Ni(OH)_2$/FeOOH@NiFe nanosheet catalysts toward highly efficient oxygen evolution reaction with ultralong stability over 1000 hours. *ACS Sustainable Chem. Eng.* **2019**, *7*, 14601−14610.

[22] Liu, T. Y.; Diao, P.; Lin, Z.; Wang, H. L. Sulfur and selenium doped nickel chalcogenides as efficient and stable electrocatalysts for hydrogen evolution reaction: The importance of the dopant atoms in and beneath the surface. *Nano Energy* **2020**, *74*, 104787.

[23] Feng, L. L.; Yu, G. T.; Wu, Y. Y.; Li, G. D.; Li, H.; Sun, Y. H.; Asefa, T.; Chen, W.; Zou, X. X. High-index faceted Ni_3S_2 nanosheet arrays as highly active and ultrastable electrocatalysts for water splitting. *J. Am. Chem. Soc.* **2015**, *137*, 14023–14026.

[24] Zhang, X. Y.; Zhang, S.; Li, J.; Wang, E. K. One-step synthesis of well-structured NiS–$Ni_2P_2S_6$ nanosheets on nickel foam for efficient overall water splitting. *J. Mater. Chem. A* **2017**, *5*, 22131–22136.

[25] Ansovini, D.; Jun Lee, C. J.; Chua, C. S.; Ong, L. T.; Tan, H. R.; Webb, W. R.; Raja, R.; Lim, Y. F. A highly active hydrogen evolution electrocatalyst based on a cobalt–nickel sulfide composite electrode. *J. Mater. Chem. A* **2016**, *4*, 9744–9749.

[26] Xue, N.; Lin, Z.; Li, P. K.; Diao, P.; Zhang, Q. F. Sulfur-doped $CoSe_2$ porous nanosheets as efficient electrocatalysts for the hydrogen evolution reaction. *ACS Appl. Mater. Interfaces* **2020**, *12*, 28288–28297.

[27] Alexander, A. M.; Hargreaves, J. S. J. Alternative catalytic materials: Carbides, nitrides, phosphides and amorphous boron alloys. *Chem. Soc. Rev.* **2010**, *39*, 4388–4401.

[28] Jiang, P.; Liu, Q.; Liang, Y. H.; Tian, J. Q.; Asiri, A. M.; Sun, X. P. A cost-effective 3D hydrogen evolution cathode with high catalytic activity: FeP nanowire array as the active phase. *Angew. Chem., Int. Ed.* **2014**, *53*, 12855–12859.

[29] Schalenbach, M.; Tjarks, G.; Carmo, M.; Lueke, W.; Mueller, M.; Stolten, D. Acidic or alkaline? Towards a new perspective on the efficiency of water electrolysis. *J. Electrochem. Soc.* **2016**, *163*, F3197–F3208.

[30] Louie, M. W.; Bell, A. T. An investigation of thin-film Ni-Fe oxide catalysts for the electrochemical evolution of oxygen. *J. Am. Chem. Soc.* **2013**, *135*, 12329–12337.

[31] Gong, M.; Li, Y. G.; Wang, H. L.; Liang, Y. Y.; Wu, J. Z.; Zhou, J. G.; Wang, J.; Regier, T.; Wei, F.; Dai, H. J. An advanced Ni-Fe layered double hydroxide electrocatalyst for water oxidation. *J. Am. Chem. Soc.* **2013**, *135*, 8452–8455.

[32] Long, X.; Li, J. K.; Xiao, S.; Yan, K. Y.; Wang, Z. L.; Chen, H. N.; Yang, S. H. A strongly coupled graphene and FeNi double hydroxide hybrid as an excellent electrocatalyst for the oxygen evolution reaction. *Angew. Chem., Int. Ed.* **2014**, *53*, 7584–7588.

[33] Lu, Z. Y.; Xu, W. W.; Zhu, W.; Yang, Q.; Lei, X. D.; Liu, J. F.; Li, Y. P.; Sun, X. M.; Duan, X. Three-dimensional NiFe layered double hydroxide film for high-efficiency oxygen evolution reaction. *Chem. Commun.* **2014**, *50*, 6479–6482.

[34] An, L.; Huang, L.; Zhou, P. P.; Yin, J.; Liu, H. Y.; Xi, P. X. A self-standing high-performance hydrogen evolution electrode with nanostructured $NiCo_2O_4$/CuS heterostructures. *Adv. Funct. Mater.* **2015**, *25*, 6814–6822.

[35] Shao, Y. B.; Zheng, M. Y.; Cai, M. M.; He, L.; Xu, C. L. Improved electrocatalytic performance of core-shell NiCo/$NiCoO_x$ with amorphous FeOOH for oxygen-evolution reaction. *Electrochim. Acta* **2017**, *257*, 1–8.

[36] Feng, J. X.; Xu, H.; Dong, Y. T.; Ye, S. H.; Tong, Y. X.; Li, G. R. FeOOH/Co/FeOOH hybrid nanotube arrays as high-performance electrocatalysts for the oxygen evolution reaction. *Angew. Chem., Int. Ed.* **2016**, *55*, 3694–3698.

[37] Diaz-Morales, O.; Ledezma-Yanez, I.; Koper, M. T. M.; Calle-Vallejo, F. Guidelines for the rational design of Ni-based double hydroxide electrocatalysts for the oxygen evolution reaction. *ACS Catal.* **2015**, *5*, 5380–5387.

[38] Elakkiya, R.; Ramkumar, R.; Maduraiveeran, G. Flower-like nickel-cobalt oxide nanomaterials as bi-functional catalyst for electrochemical water splitting. *Mater. Res. Bull.* **2019**, *116*, 98–105.

[39] Yin, J.; Zhou, P. P.; An, L.; Huang, L.; Shao, C. W.; Wang, J.; Liu, H. Y.; Xi, P. X. Self-supported nanoporous $NiCo_2O_4$ nanowires with cobalt-nickel layered oxide nanosheets for overall water splitting. *Nanoscale* **2016**, *8*, 1390–1400.

[40] Xiao, C. L.; Li, Y. B.; Lu, X. Y.; Zhao, C. Bifunctional porous NiFe/$NiCo_2O_4$/Ni foam electrodes with triple hierarchy and double synergies for efficient whole cell water splitting. *Adv. Funct. Mater.* **2016**, *26*, 3515–3523.
[41] Wang, L.; Lin, C.; Zhang, F. X.; Jin, J. Phase transformation guided single-layer β-$Co(OH)_2$ nanosheets for pseudocapacitive electrodes. *ACS Nano* **2014**, *8*, 3724–3734.
[42] Burke, M. S.; Enman, L. J.; Batchellor, A. S.; Zou, S. H.; Boettcher, S. W. Oxygen evolution reaction electrocatalysis on transition metal oxides and (oxy)hydroxides: Activity trends and design principles. *Chem. Mater.* **2015**, *27*, 7549–7558.
[43] Wang, Z. C.; Liu, H. L.; Ge, R. X.; Ren, X.; Ren, J.; Yang, D. J.; Zhang, L. X.; Sun, X. P. Phosphorus-doped Co_3O_4 nanowire array: A highly efficient bifunctional electrocatalyst for overall water splitting. *ACS Catal.* **2018**, *8*, 2236–2241.
[44] Wang, J.; Xu, F.; Jin, H. Y.; Chen, Y. Q.; Wang, Y. Non-noble metal-based carbon composites in hydrogen evolution reaction: Fundamentals to applications. *Adv. Mater.* **2017**, *29*, 1605838.
[45] Jia, Y.; Zhang, L. Z.; Gao, G. P.; Chen, H.; Wang, B.; Zhou, J. Z.; Soo, M. T.; Hong, M.; Yan, X. C.; Qian, G. R. et al. A heterostructure coupling of exfoliated Ni-Fe hydroxide nanosheet and defective graphene as a bifunctional electrocatalyst for overall water splitting. *Adv. Mater.* **2017**, *29*, 1700017.
[46] Xue, N.; Diao, P. Composite of few-layered MoS_2 grown on carbon black: Tuning the ratio of terminal to total sulfur in MoS_2 for hydrogen evolution reaction. *J. Phys. Chem. C* **2017**, *121*, 14413–14425.
[47] Bo, X.; Li, Y. B.; Hocking, R. K.; Zhao, C. NiFeCr hydroxide holey nanosheet as advanced electrocatalyst for water oxidation. *ACS Appl. Mater. Interfaces* **2017**, *9*, 41239–41245.
[48] Gong, M.; Zhou, W.; Kenney, M. J.; Kapusta, R.; Cowley, S.; Wu, Y. P.; Lu, B. A.; Lin, M. C.; Wang, D. Y.; Yang, J. et al. Blending Cr_2O_3 into a NiO-Ni electrocatalyst for sustained water splitting. *Angew. Chem., Int. Ed.* **2015**, *54*, 11989–11993.
[49] Ye, W.; Fang, X. Y.; Chen, X. B.; Yan, D. P. A three-dimensional nickel-chromium layered double hydroxide micro/nanosheet array as an efficient and stable bifunctional electrocatalyst for overall water splitting. *Nanoscale* **2018**, *10*, 19484–19491.
[50] Yang, Y.; Dang, L. N.; Shearer, M. J.; Sheng, H. Y.; Li, W. J.; Chen, J.; Xiao, P.; Zhang, Y. H.; Hamers, R. J.; Jin, S. Highly active trimetallic NiFeCr layered double hydroxide electrocatalysts for oxygen evolution reaction. *Adv. Energ. Mater.* **2018**, *8*, 1703189.
[51] Dong, C. L.; Yuan, X. T.; Wang, X.; Liu, X. Y.; Dong, W. J.; Wang, R. Q.; Duan, Y. H.; Huang, F. Q. Rational design of cobalt–chromium layered double hydroxide as a highly efficient electrocatalyst for water oxidation. *J. Mater. Chem. A* **2016**, *4*, 11292–11298.
[52] Zhang, L.; Li, Y. Y.; Peng, J. H.; Peng, K. Bifunctional $NiCo_2O_4$ porous nanotubes electrocatalyst for overall water-splitting. *Electrochim. Acta* **2019**, *318*, 762–769.
[53] Pope, C. G. X-ray diffraction and the Bragg equation. *J. Chem. Educ.* **1997**, *74*, 129.
[54] Seabold, J. A.; Choi, K. S. Efficient and stable photo-oxidation of water by a bismuth vanadate photoanode coupled with an iron oxyhydroxide oxygen evolution catalyst. *J. Am. Chem. Soc.* **2012**, *134*, 2186–2192.
[55] Gao, X. H.; Zhang, H. X.; Li, Q. G.; Yu, X. G.; Hong, Z. L.; Zhang, X. W.; Liang, C. D.; Lin, Z. Hierarchical $NiCo_2O_4$ hollow microcuboids as bifunctional electrocatalysts for overall water-splitting. *Angew. Chem., Int. Ed.* **2016**, *55*, 6290–6294.
[56] Peng, S. J.; Gong, F.; Li, L. L.; Yu, D. S.; Ji, D. X.; Zhang, T. R.; Hu, Z.; Zhang, Z. Q.; Chou, S. L.; Du, Y. H. et al. Necklace-like multishelled hollow spinel oxides with oxygen vacancies for efficient water electrolysis. *J. Am. Chem. Soc.* **2018**, *140*, 13644–13653.
[57] Ha, Y.; Shi, L. X.; Yan, X. X.; Chen, Z. L.; Li, Y. P.; Xu, W.; Wu, R. B. Multifunctional electrocatalysis on a porous N-doped $NiCo_2O_4$@C Nanonetwork. *ACS Appl. Mater. Interfaces* **2019**, *11*, 45546–45553.
[58] Deng, J.; Zhang, H. J.; Zhang, Y.; Luo, P.; Liu, L.; Wang, Y. Striking hierarchical urchin-like peapoded $NiCo_2O_4$@C as advanced bifunctional electrocatalyst for overall water splitting. *J. Power Sources* **2017**, *372*, 46–53.
[59] Wang, L. Y.; Gu, C. D.; Ge, X.; Zhang, J. L.; Zhu, H. Y.; Tu, J. P. A $NiCo_2O_4$ shell on a hollow Ni Nanorod array core for water splitting with enhanced electrocatalytic performance. *ChemNanoMat* **2018**, *4*, 124–131.
[60] Zhang, B.; Zhang, X. M.; Wei, Y.; Xia, L.; Pi, C. R.; Song, H.; Zheng, Y.; Gao, B.; Fu, J. J.; Chu, P. K. General synthesis of NiCo alloy nanochain arrays with thin oxide coating: A highly efficient bifunctional electrocatalyst for overall water splitting. *J. Alloy. Compd.* **2019**, *797*, 1216–1223.
[61] Liu, W. X.; Yu, L. H.; Yin, R. L.; Xu, X. L.; Feng, J. X.; Jiang, X.; Zheng, D.; Gao, X. L.; Gao, X. B.; Que, W. B. et al. Non-3d metal modulation of a 2D Ni-Co heterostructure array as multifunctional electrocatalyst for portable overall water splitting. *Small* **2020**, *16*, 1906775.
[62] Peng, Z.; Jia, D. S.; Al-Enizi, A. M.; Elzatahry, A. A.; Zheng, G. F. From water oxidation to reduction: Homologous Ni-Co based nanowires as complementary water splitting electrocatalysts. *Adv. Energ. Mater.* **2015**, *5*, 1402031.
[63] Du, X. Q.; Fu, J. P.; Zhang, X. S. $NiCo_2O_4$@$NiMoO_4$ supported on nickel foam for electrocatalytic water splitting. *ChemCatChem* **2018**, *10*, 5533–5540.
[64] Zhao, D. P.; Dai, M. Z.; Liu, H. Q.; Chen, K. F.; Zhu, X. F.; Xue, D. F.; Wu, X.; Liu, J. P. Sulfur-induced interface engineering of hybrid $NiCo_2O_4$@$NiMo_2S_4$ structure for overall water splitting and flexible hybrid energy storage. *Adv. Mater. Interfaces* **2019**, *6*, 1901308.
[65] Wang, Z. Q.; Zeng, S.; Liu, W. H.; Wang, X. W.; Li, Q. W.; Zhao, Z. G.; Geng, F. X. Coupling molecularly ultrathin sheets of NiFe-layered double hydroxide on $NiCo_2O_4$ nanowire arrays for highly efficient overall water-splitting activity. *ACS Appl. Mater. Interfaces* **2017**, *9*, 1488–1495.
[66] Li, M.; Tao, L. M.; Xiao, X.; Lv, X. W.; Jiang, X. X.; Wang, M. K.; Peng, Z. Q.; Shen, Y. Core-shell structured $NiCo_2O_4$@FeOOH nanowire arrays as bifunctional electrocatalysts for efficient overall water splitting. *ChemCatChem* **2018**, *10*, 4119–4125.
[67] Ren, J. T.; Yuan, G. G.; Weng, C. C.; Chen, L.; Yuan, Z. Y. Uniquely integrated Fe-doped $Ni(OH)_2$ nanosheets for highly efficient oxygen and hydrogen evolution reactions. *Nanoscale* **2018**, *10*, 10620–10628.
[68] Liu, D. N.; Lu, Q.; Luo, Y. L.; Sun, X. P.; Asiri, A. M. $NiCo_2S_4$ nanowires array as an efficient bifunctional electrocatalyst for full water splitting with superior activity. *Nanoscale* **2015**, *7*, 15122–15126.
[69] Sivanantham, A.; Ganesan, P.; Shanmugam, S. Hierarchical $NiCo_2S_4$ nanowire arrays supported on Ni foam: An efficient and durable bifunctional electrocatalyst for oxygen and hydrogen evolution reactions. *Adv. Funct. Mater.* **2016**, *26*, 4661–4672.
[70] Roffi, T. M.; Uchida, K.; Nozaki, S. Structural, electrical, and optical properties of $Co_xNi_{1-x}O$ films grown by metalorganic chemical vapor deposition. *J. Cryst. Growth* **2015**, *414*, 123–129.
[71] Venkatesh, R.; Dhas, C. R.; Sivakumar, R.; Dhandayuthapani, T.; Sudhagar, P.; Sanjeeviraja, C.; Raj, A. M. E. Analysis of optical dispersion parameters and electrochromic properties of manganese-doped Co_3O_4 dendrite structured thin films. *J. Phys. Chem. Solids* **2018**, *122*, 118–129.